Spontaneous Valley Spirals in Magnetically Encapsulated Twisted Bilayer Graphene

Tobias M. R. Wolf [ID],[1] Oded Zilberberg [ID],[1] Gianni Blatter [ID],[1] and Jose L. Lado [ID][2]

[1]*Institute for Theoretical Physics, ETH Zurich, 8093 Zurich, Switzerland*
[2]*Department of Applied Physics, Aalto University, 00076 Aalto, Espoo, Finland*
(Dated: August 17, 2020)

Van der Waals heterostructures provide a rich platform for emergent physics due to their tunable hybridization of electronic orbital- and spin-degrees of freedom. Here, we show that a heterostructure formed by twisted bilayer graphene sandwiched between ferromagnetic insulators develops flat bands stemming from the interplay between twist, exchange proximity and spin-orbit coupling. We demonstrate that in this flat-band regime, the spin degree of freedom is hybridized, giving rise to an effective triangular superlattice with valley as a degenerate pseudospin degree of freedom. Incorporating electronic interactions at half-filling leads to a spontaneous valley-mixed state, i.e., a correlated state in the valley sector with geometric frustration of the valley spinor. We show that an electric interlayer bias generates an artificial valley–orbit coupling in the effective model, controlling both the valley anisotropy and the microscopic details of the correlated state, with both phenomena understood in terms of a valley-Heisenberg model with easy-plane anisotropic exchange. Our results put forward twisted graphene encapsulated between magnetic van der Waals heterostructures as platforms to explore purely valley-correlated states in graphene.

Twisted graphene multilayers have risen as a paradigmatic platform for engineering correlated states of matter. Their unique flexibility stems from the emergence of a tunable length scale, the moiré length, which generates electronic spectral minibands with a controllable ratio between the kinetic and interaction energies. As a result, a variety of strongly-correlated states appear in these twisted van der Waals materials, such as intrinsic superconductivity [1–3], strange metal behavior [4], and correlated insulators [5]. Furthermore, this platform can realize correlated states that are rarely found in nature, such as ferromagnetic superconductivity [6] and interaction-driven quantum anomalous Hall effect [7].

The correlated states in twisted graphene multilayers that were explored thus far mostly focus on spontaneous symmetry-breaking of the spin ($\pm 1/2$) degree of freedom, i.e., of the symmetry group $SU(2)_s$ [8]. Interestingly, low-energy charge carriers in graphene also have two valleys (K, K') as a well-defined (spinor) quantum number with (approximate $SU(2)_v$ [9–12] or) $U(1)_v$ symmetry, which offers additional possibilities for spontaneous symmetry breaking due to interactions, e.g., spontaneous valley-polarized ground states [7]. So far, however, interaction-induced valley spatial textures have not been considered. Here, we show that proximity-induced spin–orbit coupling can lock spin- and orbital degrees of freedom in a way that generates exotic symmetry breaking in the valley sector when electronic interactions are included.

Spin–orbit coupling effects in monolayer graphene lead to the emergence of the quantum anomalous Hall effect [13, 14]. They are tuned experimentally using electric fields [15] and by proximity to semiconductors [16]. Note that Rashba SOC effects can be on the order of 0.1 meV in single-layer graphene encapsulated in Boron-Nitride [15], 0.3 meV in hydrogenated graphene [17], and up to 1.5 meV for graphene on dichalcogenides [16, 18]. Moving to twisted graphene bilayers, this energy scale should be compared with a typical Coulomb correlation gap of ~ 0.3 meV [5]. Remarkably, even though the Rashba SOC can compete with these correlated gaps, this in-
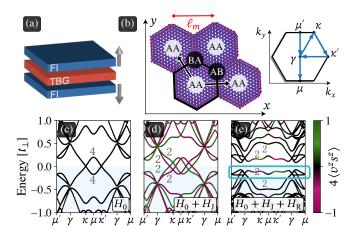

FIG. 1. Structure and single-particle electronic properties of twisted bilayer graphene (TBG) encapsulated within ferromagnetic insulators (FI). (a) Sketch of the encapsulated system, where arrows denote the magnetization orientation of each FI. (b) Moiré spatial pattern arising from stacking two graphene layers with relative twist angle α. The pattern has a length scale ℓ_m with characteristic AA, AB, and BA regions. It generates a hexagonal mini-Brillouin zone with characteristic high-symmetry points. (c-e) Bandstructures at twist angle $\alpha \simeq 2°$, interlayer coupling $t_\perp = 0.12t$, and no interlayer bias ($V = 0$) along the high-symmetry path γ–κ–κ'–γ–μ: for the isolated TBG (c), including local exchange fields with $m = t_\perp/3$ (d), and including both local exchange fields with $m = t_\perp/3$ and Rashba SOC $\lambda_R = t_\perp/3$ (e). The coloring of the bands indicates the expectation value of the valley–spin operator $\langle v^z s^z \rangle$, showing fixed spin and valley in (d) and finite spin-mixing at fixed valley in (e). The light-blue box marks the flat band below charge neutrality.

terplay has thus far not received much attention in twisted van der Waals materials.

In this work, we focus on the valley degree of freedom, described as a two-spinor, and demonstrate the emergence of correlations in the valley spinor of twisted bilayer graphene encapsulated within ferromagnetic insulators (FIs), such as CrI$_3$, see Fig. 1(a). We show that the combination of twist

engineering alongside proximity-induced magnetic exchange and Rashba spin–orbit coupling hybridizes the spin degree of freedom and leads to valley-degenerate flat bands. It is this valley-degeneracy in the absence of spin-degeneracy that provides us with a unique playground for symmetry-broken states solely in the valley sector. To describe the latter, we propose a phenomenological triangular lattice model that captures the low-energy flat-band valley-physics. At half-filling of the flat bands, we find that screened Coulomb interactions lead to a symmetry breaking with valley-spiral order. Furthermore, we find that the latter is described by an anisotropic valley-Heisenberg model and that the easy-axis anisotropic valley-exchange can be controlled through electric interlayer bias. Finally, we discuss potential experimental scenarios to detect this effect.

Our system consists of twisted bilayer graphene encapsulated in the z-direction between ferromagnetic insulators, see Fig. 1(a). We describe the electronic properties of the system using an effective atomistic tight-binding Hamiltonian for the graphene bilayer

$$H = H_0 + H_J + H_R, \qquad (1)$$

where the electronic degrees of freedom of the FI are integrated out. The Hamiltonian H_0 describes the bare twisted bilayer, H_J includes proximity-induced exchange fields (induced by virtual tunneling processes between the bilayer and the FI) [14, 19–24], and H_R contributes a Rashba spin–orbit coupling that stems from a combination of proximity-induced spin–orbit coupling and locally-broken mirror symmetry [16, 18, 25]. The bare Hamiltonian of the bilayer reads $H_0 = \sum_{\langle i,j \rangle, s} t\, c_{i,s}^\dagger c_{j,s} + \sum_{i,j,s} t_{ij}^\perp c_{i,s}^\dagger c_{j,s} - \sum_{i,s} V_i\, c_{i,s}^\dagger c_{i,s}$, where $c_{i,s}^{(\dagger)}$ destroys (creates) an electron with spin $s \in \{\pm 1/2\}$ at position $\mathbf{r}_i = (x_i, y_i, z_i)$ in one of the layers located at $z_i = \pm d/2$. We consider intralayer nearest-neighbor hopping with amplitude $t \simeq 2.7\,\text{eV}$ [26]. The interlayer hopping from site $\mathbf{r}_i$ to $\mathbf{r}_j$ is parametrized as $t_{ij}^\perp = t_\perp [(z_i - z_j)^2 / |\mathbf{r}_i - \mathbf{r}_j|^2]\, e^{-(|\mathbf{r}_i - \mathbf{r}_j| - d)/\ell}$ with $t_\perp \simeq 0.12\,t$ that describes the hybridization over the interlayer distance $d \simeq 2.35 a_0$ with a_0 the intralayer bond length and $\ell \simeq 0.3\,a_0$ controlling the interlayer hopping range [27–29]. The onsite potentials $V_i = \mu + \text{sgn}(z_i)V$ describe the overall chemical potential μ and electric interlayer bias V.

We first discuss the system in the absence of interlayer bias, $V = 0$. Each isolated graphene layer $l \in \{1, 2\}$ exhibits a characteristic spectrum with Dirac-like band touchings at valleys K, K' [26], which we label with the eigenvalues $v \in \{\pm 1/2\}$ of the valley operator v^z, respectively [30–33]. Consequently, the decoupled bilayer has spectral bands that are eightfold degenerate, characterized by layer, valley, and spin indices, $|l, v, s\rangle$, respectively. Interlayer coupling ($t_\perp \neq 0$), mixes the energy bands between the layers. Furthermore, a twist angle α between the layers leads to a moiré superlattice structure with a characteristic distance ℓ_m and regions labeled AA- and AB/BA in accord with the alignment of the A and B sites of each graphene layer on top of each other, see Fig. 1(b). The resulting large superstructure implies that the electronic spec-

trum of H_0 consists of many minibands, resulting from back-folding the dispersion of each graphene layer and subsequent hybridization by the interlayer coupling [34], see Fig. 1(c). For a large moiré length ℓ_m and low energies, intervalley scattering can be neglected, i.e., $t_\perp$ does not couple different valleys. As a result, each miniband at Bloch momentum $\mathbf{k}$ (corresponding to valley K) is degenerate in spin and has a valley-partner at $-\mathbf{k}$ (corresponding to valley K'). Hence, each eigenvalue is at least four-fold degenerate [35–39], or higher along high-symmetry lines in the mini-Brillouin zone (mBZ). Crucially, except for fine-tuned angles [33, 36, 38, 40–43] or in the limit of tiny twist angles [31, 39], the low-energy minibands are typically dispersive.

The encapsulation of the TBG between ferromagnetic insulators with magnetization pointing out of plane (and an antiferromagnetic alignment between the FIs) [cf. Fig. 1(a)] profoundly alters the low-energy spectrum. In this configuration, the FIs induce exchange fields with effective moment $\mathbf{m}_i = \text{sgn}(z_i)m\hat{z}$ at each site $\mathbf{r}_i$, and the locally-broken mirror symmetry generates Rashba spin–orbit coupling $\lambda_{R,i} = \text{sgn}(z_i)\lambda_R$ in each graphene layer [44]. These effects are, respectively, described by $H_J = \sum_{j,ss'} (\mathbf{m}_j \cdot \boldsymbol{\sigma})_{ss'}\, c_{j,s}^\dagger c_{j,s'}$, and $H_R = i \sum_{\langle i,j \rangle, ss'} \lambda_{R,i} (\boldsymbol{\sigma} \times \mathbf{d}_{ij})_{ss'}^z\, c_{i,s}^\dagger c_{j,s'}$, where $\mathbf{d}_{ij}$ is the bond vector connecting intralayer sites i, j, and the components of $\boldsymbol{\sigma} = (\sigma^x, \sigma^y, \sigma^z)$ are the Pauli matrices describing spin. As we assume the two FI layers to be antiferromagnetically-aligned along the z-axis, the induced exchange fields act as a (spin-dependent) magnetic interlayer bias [45]. Interestingly, even though the exchange field $\mathbf{m}_i$ breaks time-reversal symmetry, the eigenstates remain spin degenerate, see Fig. 1(d). This is a result of the symmetric orbital distribution between the layers, i.e., the spin-↑ bands of one layer remain degenerate with the spin-↓ bands of the other (and vice versa), while the interlayer coupling does not mix spins. The Rashba coupling term λ_R, however, mixes the two spin channels, introduces a sizeable hybridization gap around charge neutrality, and flattens-out the otherwise dispersive bands, see Fig. 1(e).

As a result, the FI-encapsulated twisted bilayer features a pronounced van Hove singularity adjacent to the energy gap at charge neutrality. This singularity becomes most pronounced for a fine-tuned value of the ratio $\alpha/t_\perp$ between twist angle and the interlayer coupling, here corresponding to physical parameters $\alpha \approx 2°$, $t_\perp = 0.12t$, when $m = t_\perp/3$, $\lambda_R = t_\perp/3$ [46]. The corresponding bands then become maximally flat, see Fig. 1(e), and their wavefunctions are mostly concentrated within the AA region of the moiré unit cell, see Fig. 2(a). Importantly, these bands are only two-fold degenerate in the *valley* degree of freedom, whereas spin degeneracy is fully broken – in contrast with other graphene multilayer systems, where spin- and layer-degeneracies persist [37].

Crucial to our work, these low-energy flat bands resemble a simple effective model for hopping between Wannier moiré orbitals arranged in a triangular superlattice, see Fig. 2(b), i.e.,

$$\mathcal{H}_0 = \sum_{\langle IJ \rangle} \gamma_1\, \psi_I^\dagger e^{i\sigma^z v_{IJ}\phi_1} \psi_J + \sum_{\langle\langle IJ \rangle\rangle} \gamma_2\, \psi_I^\dagger e^{i\sigma^z v_{IJ}\phi_2} \psi_J, \qquad (2)$$
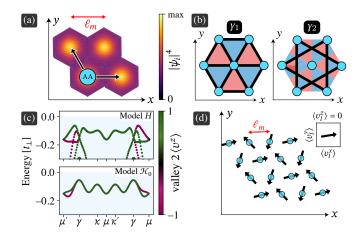
FIG. 2. Effective triangular lattice model for the moiré orbitals of the flat band. (a) Local density of states of the flat band below charge neutrality highlighted in Fig. 1(e). (b) A sketch of the triangular lattice model $\mathcal{H}_0$, see Eq. (2), where cyan circles represent the AA regions, the black lines denote first- and second-neighbors hoppings γ_1, γ_2 respectively, and the red/blue triangles represent the staggered flux patterns associated with the phases ϕ_1 and ϕ_2 for first- and second-neighbor hopping. (c, top) Close-up on the flat band in Fig. 1(e), and (c, bottom) comparison with the band of the phenomenological model [cf. Eq. (2) with $\gamma_1/t_\perp = 0.03$, $\gamma_2/t_\perp = 0.09$, $\phi_1 = 0$, $\phi_2 = -0.4$]. The band color indicates the valley index $v = \langle v^z \rangle$ and illustrates the valley-degeneracy along γ–κ–κ'–γ (green on top of magenta). (d) (In-plane) valley spiral appearing in the mean field ground state of $\mathcal{H}_0 + \mathcal{H}_U$, cf. Eqs. (2) and (3). Arrows illustrate the valley polarization $\langle \boldsymbol{v}_I \rangle$ of the respective orbital (inset).

with the valley spinors $\psi_I^{(\dagger)} = (d_{I,1/2}^{(\dagger)}, d_{I,-1/2}^{(\dagger)})$ and destruction (creation) operators $d_{I,v}^{(\dagger)}$ for electrons on moiré unit cells I with valley index v taking the role of a pseudospin. The form of the hopping amplitudes follows from symmetry arguments [46], and we include first- and second-neighbor amplitudes $\gamma_{1,2} > 0$ with phases $\phi_{1,2}$, and signs $\nu_{IJ} = -\nu_{JI} \in \{\pm 1\}$ that ensure symmetry under rotation by $2\pi/3$, see Fig. 2(b). Similar complex-valued hopping amplitudes appear in the Kane-Mele model [47] due to spin–orbit coupling, such that we refer to $\phi_{1,2}$ as 'valley–orbit phases' in our model by analogy. In the absence of interlayer bias, symmetry enforces real first-neighbor hopping ($\phi_1 = 0$) [46], whereas ϕ_2 is finite in general. The hopping parameters can then be chosen to qualitatively reproduce the flat band, see Fig. 2(c). We will see how interlayer bias affects this low-energy valley-spinor model later.

The presence of a van Hove singularity (flat bands) naturally raises the question how interactions affect the corresponding electronic states near half-filling of the flat band. In the bilayer, this corresponds to doping the system with one electron/hole per moiré unit cell. Coulomb interactions in the microscopic model (1) lead to effective Coulomb interactions between the moiré orbitals in the low-energy model (2). Assuming that the screened Coulomb interaction between the atoms is shorter-ranged than the moiré length scale ℓ_m [48], the effective inter-

action between the moiré orbitals becomes

$$\mathcal{H}_U = \frac{U}{2} \sum_{I,v} n_{I,v} n_{I,-v}, \tag{3}$$

where $n_{I,v} = d_{I,v}^\dagger d_{I,v}$ is the number operator for valley v of the moiré orbital I and $U \simeq 0.15 t_\perp$ [48] is the Hubbard interaction strength. Our effective model $\mathcal{H} = \mathcal{H}_0 + \mathcal{H}_U$ differs from the conventional Fermi-Hubbard model [49] in two respects: First, we have valley as pseudospin, and second, our hopping amplitudes are complex. In what follows, we consider half-filling such that the expected occupation number is $\langle n_I \rangle = 1$, and calculate the valley order of the ground state of $\mathcal{H}$. Analogous to spin order, we characterize valley order by the expectation value of the valley operator $\boldsymbol{v}_I = \psi_I^\dagger \boldsymbol{\sigma} \psi_I / 2$ in each moiré cell I. We can interpret $\langle v_I^z \rangle$ as the local valley imbalance and $\langle v_I^{x,y} \rangle$ as local valley coherence. We will see that, similar to other spin-1/2 triangular lattice models [50–53], our model $\mathcal{H}$, cf. Eqs. (2) and (3), is prone to valley-spiral states [see Fig. 2(d)], and that valley–orbit coupling, i.e., our complex-valued hoppings, can promote anisotropic exchange [51].

We determine the ground state using a self-consistent mean-field approximation for the many-body interaction, $\mathcal{H}_U \approx \sum_I \psi_I^\dagger \bar{U}(\rho^I) \psi_I - E_0(\rho^I)$, where we introduced the density matrix $\rho^I = (\langle n_I \rangle + \langle \boldsymbol{v}_I \rangle \cdot \boldsymbol{\sigma})/2$ and the mean-field interaction $\bar{U}(\rho^I)$ and shift $E_0(\rho^I)$ [46]. Performing self-consistent relaxation of different initial states, we find that interactions and geometrical frustration in the triangular lattice favor a valley-spiral state on the length scale of the moiré structure, see Fig. 2(d). We find that (i) the length scale of the spiral varies slightly with the ratio γ_2/γ_1, and (ii) that the spiral favors planar configurations with $\langle v_I^z \rangle = 0$. Hence, the valleys seek a state with equal occupation $\langle n_{I,K} \rangle = \langle n_{I,K'} \rangle$ and mix coherently, $\langle v_I^{x,y} \rangle \neq 0$. Interestingly, in the limit $\phi_2 \to 0$, stabilization of the in-plane spiral state is lost such that spiral states with finite out-of-plane components $\langle v_I^z \rangle > 0$ become degenerate with in-plane spiral configurations; this suggests that the phases ϕ_1 and ϕ_2 in $\mathcal{H}_0$ [see Eq. (2) and Fig. 2(b)] play a crucial role in defining the valley order.

To better understand our mean-field results, we expand the Hamiltonian $\mathcal{H}$ at half-filling in the strong-interaction limit $U \gg \gamma_1, \gamma_2$ using a Schrieffer-Wolff transformation [46, 54] that takes us to a valley-Heisenberg model with anisotropic and (anti-)symmetric exchange, i.e.,

$$\mathcal{H}_v = \sum_{IJ} J_{IJ} \boldsymbol{v}_I \cdot \boldsymbol{v}_J + \Delta_{IJ} v_I^z v_J^z + \nu_{IJ} D_{IJ} (\boldsymbol{v}_I \times \boldsymbol{v}_J)_z. \tag{4}$$

Here, J_{IJ}, Δ_{IJ}, and D_{IJ} denote the isotropic, anisotropic, and antisymmetric exchange couplings, respectively. These couplings are finite for first- and second-neighbor exchange only (indexed by $n = 1, 2$) and take the form $J_n = J_n^0 (\cos^2 \phi_n - \sin^2 \phi_n)$, $\Delta_n = 2J_n^0 \sin^2 \phi_n$, and $D_n = J_n^0 \sin(2\phi_n)$, with $J_n^0 = 2\gamma_n^2/U$. In the absence of an interlayer bias ($V = 0$), we have $\phi_1 = 0$ such that the first-neighbor terms in $\mathcal{H}_v$ are isotropic. Generally, the isotropic exchange couplings J_n can turn valleymagnetic [55] ($J_n < 0$) as ϕ_n increases; however, for
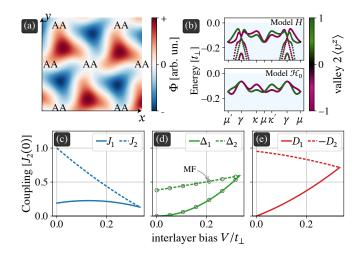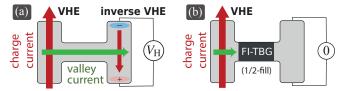
FIG. 4. Schematic setup for an experiment signaling the presence of a valley spiral state. (a) Standard four-terminal device, with valley Hall effect (VHE) driven by a charge current and inverse VHE driven by a valley current and producing a finite voltage V_H [59, 60]. (b) FI-encapsulated TBG (FI-TBG) at half-filling of the flat band acts as filter blocking the valley current and suppresses the voltage V_H of the inverse VHE.

FIG. 3. Effect of interlayer bias V on single-particle properties and effective valley–valley exchange interactions in the anisotropic valley-Heisenberg model $\mathcal{H}_v$ (4). (a) Local valley (Berry) flux $\Phi(\boldsymbol{r}, E)$ near half-filling (at energy $E \simeq -0.1t_\perp$), averaged over the microscopic scale of model (1) including both layers, see Eq. 5. The staggered flux is largest in AB/BA regions and vanishes in the AA regions. (b) Flat band as obtained from the microscopic model (1) (top panel) compared with the phenomenological model (2) (bottom panel) at finite interlayer bias $V = 0.33t_\perp$, and with $\gamma_1 = \gamma_2 = 0.07t_\perp$ and $\phi_1 = -\phi_2 = 0.7$. Note the difference with the $V = 0$ result in Fig. 2(c). (c–e) Isotropic (J_n), anisotropic (Δ_n) and antisymmetric (D_n) valley exchange-couplings, cf. Eq. (4), for first and second neighbors ($n = 1, 2$) as interlayer bias V increases. The interlayer bias can enhance the first-neighbor coupling even to the point where it has the same magnitude and phase as the second-neighbor coupling (here $V \simeq 0.3t_\perp$). Panel (d) shows the numerical mean field result (open circles) superimposed on top of the analytical result (solid/dashed lines) [46].

the regimes we consider here, we can restrict ourselves to anti-valleymagnetic couplings ($J_n > 0$ for $n = 1, 2$), which favors valley spirals due geometric frustration in the triangular lattice. The finite phase ϕ_2 in the second-neighbor coupling stabilizes in-plane valley configurations by inducing anisotropy $\Delta_2 > 0$ and favors second-neighbor valley misalignment (canting) due to the antisymmetric coupling $D_2 > 0$. Note that the alternating nature of the signs $\nu_{IJ} \in \{\pm 1\}$ in our triangular lattice favors valley spirals as well, rather than chiral structures such as skyrmions [56]. Consequently, there are two distinct mechanisms driving valley spirals, such that the length scale of the valley spiral depends on the competition between anti-valleymagnetic geometric frustration (J_n, $n = 1, 2$) and the antisymmetric couplings (D_n, $n = 1, 2$). In the following, we investigate how the addition of a finite electric interlayer bias modifies the results discussed thus far.

Including a finite interlayer bias $V > 0$ in Eq. (1) induces effective valley-dependent fluxes $v\Phi(\boldsymbol{r}_i, E)$ in real space that remove the valley degeneracy, see Fig. 3(b); within the low-energy model $\mathcal{H}_0$ (2), they modify the valley–orbit phases ϕ_1 and ϕ_2. This is formalized by defining the valley flux of low-energy states [33, 57, 58] near the energy E and at position $\boldsymbol{r}_i$

as

$$\Phi(\boldsymbol{r}_i, E) = \int_{BZ} \frac{d^2\boldsymbol{k}}{(2\pi)^2} \frac{\epsilon_{\alpha\beta}}{2} \langle \boldsymbol{r}_i | G\left(\partial_{k_\alpha} G^{-1}\right)\left(\partial_{k_\beta} G\right)|\boldsymbol{r}_i\rangle, \quad (5)$$

where $G = [E - H(\boldsymbol{k}) + i0^+]^{-1}\mathcal{P}$ is the valley Green's function with valley-polarization operator $\mathcal{P} = 2v^z$, and $\epsilon_{\alpha\beta}$ denotes the Levi-Civita symbol. For our flat bands, we find that the interlayer bias induces a staggered valley flux, see Fig. 3(a). This flux can be included in the low-energy model $\mathcal{H}_0$ (2), through a Peierls substitution, i.e., $\gamma_n \mapsto \gamma_n(V)\, e^{i\sigma^z \phi_n(V)}$ for $n = 1, 2$, cf. Fig. 2(b). It contributes dominantly to ϕ_1, and provides an additional correction to ϕ_2 accounting for the tilt in the pattern. The bands of the effective model $\mathcal{H}_0(V)$ obtained in this way qualitatively agree with the bands of the atomistic tight-binding Hamiltonian (1) evaluated at a finite interlayer bias V, see Fig. 3(b).

Consequently, the interlayer bias directly controls the effective valley-exchange couplings in model $\mathcal{H}_v$ (4) through the induced valley–orbit couplings $\phi_1(V)$ and $\phi_2(V)$. In Figs. 3(c-f), we see that the couplings J_1, Δ_2, and D_2 do not change significantly with increasing bias V, while the coupling J_2 decreases substantially, and Δ_1 and D_1 both turn finite and increase appreciably. As a result, we find here that the interlayer bias (i) increases the easy-plane exchange anisotropy (increasing Δ_n), (ii) decreases the overall tendency for anti-valleymagnetic order and geometric frustration (decreasing J_n), and (iii) increases canting (through D_n). Interestingly, this means that the interlayer bias switches between the two mechanisms responsible for valley spirals. Note that there is also a competition of canting between first-neighbor and second-neighbor orbital pairs that influences the length scale of the valley spiral, where in numerical mean-field calculations we predominantly observed 120° and 60° spiral structures. A more detailed analysis of competing spiral structures is beyond the scope of this work.

In contrast to spin, valley is an orbital degree of freedom, and thus provides an extra challenge when it comes to interpretation and experimental verification of valley-physics [39, 59–68]. A promising direction is to make use of the valley Hall effect (VHE), where band electrons from valley K flow in the opposite direction as those from valley K', leading to transverse charge-neutral valley currents [59, 60, 69]. These currents

can be detected as they induce voltages in other regions of the material through the inverse-VHE, see Fig. 4(a). Such a four-terminal transport setup enables the detection of our valley-correlated state, i.e., the latter can be characterized through its action on a valley Hall measurement when embedding our system into a suitable device geometry, see Fig. 4(b). For example, a valley-magnet ($\langle v_I^z \rangle \neq 0$) acts as a valley-filter and can be used to suppress the valley Hall signal for one valley but not the other. In our case, we expect the planar valley-spiral ($\langle v_I^z \rangle = 0$) to act as a "coherent valley mixer" [70–72]. This would strongly suppress the valley Hall signal when the chemical potential is swept to approach half-filling of the flat band, thus providing an experimental signature by which to detect the valley spiral.

To conclude, our results put forward a minimal graphene-based heterostructure displaying spontaneous valley-mixing, opening up a pathway to explore valley-correlated states in twisted graphene multilayers. Going beyond this work, FI-encapsulated TBG and twisted *double*-bilayer graphene (TDBG) have analogous electronic band structures, except that spin in the former replaces the additional graphene layer in the latter. This can be understood by considering monolayer graphene on a magnetic substrate compared with isolated bilayer graphene. This similarity suggests that many recent proposals and observations [73–75] for the latter may also apply to the model studied here. In particular, besides correlated insulating states [6, 76], ferromagnetic superconductors emerge in TDBG [74], which, by extension, could lead to valleymagnetic superconductivity in our model when doped away from half-filling. Ultimately, the proposed FI-TBG can become a potential candidate to realize valley-analogous versions of fractional quantum Hall states [77–80], and quantum valley-liquids in twisted van der Waals materials [12, 81–83].

[1] Y. Cao, V. Fatemi, S. Fang, K. Watanabe, T. Taniguchi, E. Kaxiras, and P. Jarillo-Herrero, Unconventional superconductivity in magic-angle graphene superlattices, Nature **556**, 43 (2018).

[2] M. Yankowitz, S. Chen, H. Polshyn, Y. Zhang, K. Watanabe, T. Taniguchi, D. Graf, A. F. Young, and C. R. Dean, Tuning superconductivity in twisted bilayer graphene, Science **363**, 1059 (2019).

[3] X. Lu, P. Stepanov, W. Yang, M. Xie, M. A. Aamir, I. Das, C. Urgell, K. Watanabe, T. Taniguchi, G. Zhang, A. Bachtold, A. H. MacDonald, and D. K. Efetov, Superconductors, orbital magnets and correlated states in magic-angle bilayer graphene, Nature **574**, 653 (2019).

[4] Y. Cao, D. Chowdhury, D. Rodan-Legrain, O. Rubies-Bigorda, K. Watanabe, T. Taniguchi, T. Senthil, and P. Jarillo-Herrero, Strange metal in magic-angle graphene with near Planckian dissipation, Phys. Rev. Lett. **124**, 076801 (2020).

[5] Y. Cao, V. Fatemi, A. Demir, S. Fang, S. L. Tomarken, J. Y. Luo, J. D. Sanchez-Yamagishi, K. Watanabe, T. Taniguchi, E. Kaxi-

[6] ras, R. C. Ashoori, and P. Jarillo-Herrero, Correlated insulator behaviour at half-filling in magic-angle graphene superlattices, Nature **556**, 80 (2018).

[6] Y. Cao, D. Rodan-Legrain, O. Rubies-Bigorda, J. M. Park, K. Watanabe, T. Taniguchi, and P. Jarillo-Herrero, Tunable correlated states and spin-polarized phases in twisted bilayer–bilayer graphene, Nature 10.1038/s41586-020-2260-6 (2020).

[7] M. Serlin, C. L. Tschirhart, H. Polshyn, Y. Zhang, J. Zhu, K. Watanabe, T. Taniguchi, L. Balents, and A. F. Young, Intrinsic quantized anomalous Hall effect in a moiré heterostructure, Science **367**, 900 (2019).

[8] J. D. Sanchez-Yamagishi, J. Y. Luo, A. F. Young, B. M. Hunt, K. Watanabe, T. Taniguchi, R. C. Ashoori, and P. Jarillo-Herrero, Helical edge states and fractional quantum Hall effect in a graphene electron–hole bilayer, Nature Nanotechnology **12**, 118 (2016).

[9] M.-S. Choi, R. López, and R. Aguado, Su(4) Kondo effect in carbon nanotubes, Phys. Rev. Lett. **95**, 067204 (2005).

[10] P. Jarillo-Herrero, J. Kong, H. S. Van Der Zant, C. Dekker, L. P. Kouwenhoven, and S. De Franceschi, Orbital Kondo effect in carbon nanotubes, Nature **434**, 484 (2005).

[11] C. Xu and L. Balents, Topological superconductivity in twisted multilayer graphene, Phys. Rev. Lett. **121**, 087001 (2018).

[12] W. M. H. Natori, R. Nutakki, R. G. Pereira, and E. C. Andrade, SU(4) Heisenberg model on the honeycomb lattice with exchange-frustrated perturbations: Implications for twistronics and Mott insulators, Phys. Rev. B **100**, 205131 (2019).

[13] Z. Qiao, S. A. Yang, W. Feng, W.-K. Tse, J. Ding, Y. Yao, J. Wang, and Q. Niu, Quantum anomalous Hall effect in graphene from Rashba and exchange effects, Phys. Rev. B **82**, 161414 (2010).

[14] Z. Wang, C. Tang, R. Sachs, Y. Barlas, and J. Shi, Proximity-induced ferromagnetism in graphene revealed by the anomalous Hall effect, Phys. Rev. Lett. **114**, 016603 (2015).

[15] M. H. D. Guimarães, P. J. Zomer, J. Ingla-Aynés, J. C. Brant, N. Tombros, and B. J. van Wees, Controlling spin relaxation in hexagonal BN-encapsulated graphene with a transverse electric field, Phys. Rev. Lett. **113**, 086602 (2014).

[16] C. K. Safeer, J. Ingla-Aynés, F. Herling, J. H. Garcia, M. Vila, N. Ontoso, M. R. Calvo, S. Roche, L. E. Hueso, and F. Casanova, Room-temperature spin Hall effect in graphene/MoS2 van der waals heterostructures, Nano Letters **19**, 1074 (2019).

[17] M. Gmitra, D. Kochan, and J. Fabian, Spin-orbit coupling in hydrogenated graphene, Phys. Rev. Lett. **110**, 246602 (2013).

[18] B. Yang, M. Lohmann, D. Barroso, I. Liao, Z. Lin, Y. Liu, L. Bartels, K. Watanabe, T. Taniguchi, and J. Shi, Strong electron-hole symmetric Rashba spin-orbit coupling in graphene/monolayer transition metal dichalcogenide heterostructures, Phys. Rev. B **96**, 041409 (2017).

[19] D. Zhong, K. L. Seyler, X. Linpeng, R. Cheng, N. Sivadas, B. Huang, E. Schmidgall, T. Taniguchi, K. Watanabe, M. A. McGuire, W. Yao, D. Xiao, K.-M. C. Fu, and X. Xu, Van der Waals engineering of ferromagnetic semiconductor heterostructures for spin and valleytronics, Science Advances **3**, e1603113 (2017).

[20] H. X. Yang, A. Hallal, D. Terrade, X. Waintal, S. Roche, and M. Chshiev, Proximity effects induced in graphene by magnetic insulators: First-principles calculations on spin filtering and exchange-splitting gaps, Phys. Rev. Lett. **110**, 046603 (2013).

[21] S. Singh, J. Katoch, T. Zhu, K.-Y. Meng, T. Liu, J. T. Brangham, F. Yang, M. E. Flatté, and R. K. Kawakami, Strong modulation of spin currents in bilayer graphene by static and fluctuating proximity exchange fields, Phys. Rev. Lett. **118**, 187201 (2017).

[22] K. Zollner, P. E. Faria Junior, and J. Fabian, Proximity exchange

effects in MoSe$_2$ and WSe$_2$ heterostructures with CrI$_3$: Twist angle, layer, and gate dependence, Phys. Rev. B **100**, 085128 (2019).

[23] M. Peralta, E. Medina, and F. Mireles, Proximity-induced exchange and spin-orbit effects in graphene on Ni and Co, Phys. Rev. B **99**, 195452 (2019).

[24] W. Han, R. K. Kawakami, M. Gmitra, and J. Fabian, Graphene spintronics, Nature Nanotechnology **9**, 794 (2014).

[25] Y. S. Dedkov, M. Fonin, U. Rüdiger, and C. Laubschat, Rashba effect in the graphene/Ni(111) system, Phys. Rev. Lett. **100**, 107602 (2008).

[26] A. H. Castro Neto, F. Guinea, N. M. R. Peres, K. S. Novoselov, and A. K. Geim, The electronic properties of graphene, Rev. Mod. Phys. **81**, 109 (2009).

[27] S. Reich, J. Maultzsch, C. Thomsen, and P. Ordejón, Tight-binding description of graphene, Phys. Rev. B **66**, 035412 (2002).

[28] G. Trambly de Laissardière, D. Mayou, and L. Magaud, Localization of Dirac electrons in rotated graphene bilayers, Nano letters **10**, 804 (2010).

[29] P. Moon and M. Koshino, Optical absorption in twisted bilayer graphene, Phys. Rev. B **87**, 205404 (2013).

[30] E. Colomés and M. Franz, Antichiral edge states in a modified Haldane nanoribbon, Phys. Rev. Lett. **120**, 086603 (2018).

[31] A. Ramires and J. L. Lado, Electrically tunable gauge fields in tiny-angle twisted bilayer graphene, Phys. Rev. Lett. **121**, 146801 (2018).

[32] A. Ramires and J. L. Lado, Impurity-induced triple point fermions in twisted bilayer graphene, Phys. Rev. B **99**, 245118 (2019).

[33] T. M. R. Wolf, J. L. Lado, G. Blatter, and O. Zilberberg, Electrically tunable flat bands and magnetism in twisted bilayer graphene, Phys. Rev. Lett. **123**, 096802 (2019).

[34] A. O. Sboychakov, A. L. Rakhmanov, A. V. Rozhkov, and F. Nori, Electronic spectrum of twisted bilayer graphene, Phys. Rev. B **92**, 075402 (2015).

[35] J. M. B. Lopes dos Santos, N. M. R. Peres, and A. H. Castro Neto, Continuum model of the twisted graphene bilayer, Phys. Rev. B **86**, 155449 (2012).

[36] E. Suárez Morell, J. D. Correa, P. Vargas, M. Pacheco, and Z. Barticevic, Flat bands in slightly twisted bilayer graphene: Tight-binding calculations, Phys. Rev. B **82**, 121407 (2010).

[37] J. M. B. Lopes dos Santos, N. M. R. Peres, and A. H. Castro Neto, Graphene bilayer with a twist: Electronic structure, Phys. Rev. Lett. **99**, 256802 (2007).

[38] R. Bistritzer and A. H. MacDonald, Moire bands in twisted double-layer graphene, Proceedings of the National Academy of Sciences **108**, 12233 (2011).

[39] P. San-Jose and E. Prada, Helical networks in twisted bilayer graphene under interlayer bias, Phys. Rev. B **88**, 121408 (2013).

[40] M. Koshino, N. F. Q. Yuan, T. Koretsune, M. Ochi, K. Kuroki, and L. Fu, Maximally localized Wannier orbitals and the extended Hubbard model for twisted bilayer graphene, Phys. Rev. X **8**, 031087 (2018).

[41] J. Kang and O. Vafek, Symmetry, maximally localized Wannier states, and a low-energy model for twisted bilayer graphene narrow bands, Phys. Rev. X **8**, 031088 (2018).

[42] H. C. Po, L. Zou, A. Vishwanath, and T. Senthil, Origin of Mott insulating behavior and superconductivity in twisted bilayer graphene, Phys. Rev. X **8**, 031089 (2018).

[43] K. Hejazi, C. Liu, H. Shapourian, X. Chen, and L. Balents, Multiple topological transitions in twisted bilayer graphene near the first magic angle, Phys. Rev. B **99**, 035111 (2019).

[44] C. Gong and X. Zhang, Two-dimensional magnetic crystals and emergent heterostructure devices, Science **363**, 10.1126/science.aav4450 (2019).

[45] C. Cardoso, D. Soriano, N. A. García-Martínez, and J. Fernández-Rossier, Van der Waals spin valves, Phys. Rev. Lett. **121**, 067701 (2018).

[46] See supplemental material for more details on the effective model, the mean field approximation and on the anisotropic valley Heisenberg model.

[47] C. L. Kane and E. J. Mele, Quantum spin hall effect in graphene, Phys. Rev. Lett. **95**, 226801 (2005).

[48] F. Guinea and N. R. Walet, Electrostatic effects, band distortions, and superconductivity in twisted graphene bilayers, Proceedings of the National Academy of Sciences **115**, 13174 (2018).

[49] J. Hubbard, Electron correlations in narrow energy bands, Proceedings of the Royal Society of London. Series A. Mathematical and Physical Sciences **276**, 238 (1963).

[50] P. Sahebsara and D. Sénéchal, Hubbard model on the triangular lattice: Spiral order and spin liquid, Phys. Rev. Lett. **100**, 136402 (2008).

[51] A. Vaezi, M. Mashkoori, and M. Hosseini, Phase diagram of the strongly correlated Kane-Mele-Hubbard model, Phys. Rev. B **85**, 195126 (2012).

[52] K. Li, S.-L. Yu, Z.-L. Gu, and J.-X. Li, Phase diagram and topological phases in the triangular lattice Kitaev-Hubbard model, Phys. Rev. B **94**, 125120 (2016).

[53] K. Misumi, T. Kaneko, and Y. Ohta, Mott transition and magnetism of the triangular-lattice Hubbard model with next-nearest-neighbor hopping, Phys. Rev. B **95**, 075124 (2017).

[54] J. R. Schrieffer and P. A. Wolff, Relation between the Anderson and Kondo Hamiltonians, Phys. Rev. **149**, 491 (1966).

[55] We introduce the nomenclature (anti)valleymagnetic for the valley sector in distinction to (anti)ferromagnetism in the spin sector.

[56] S. Heinze, K. Von Bergmann, M. Menzel, J. Brede, A. Kubetzka, R. Wiesendanger, G. Bihlmayer, and S. Blügel, Spontaneous atomic-scale magnetic skyrmion lattice in two dimensions, Nature Physics **7**, 713 (2011).

[57] K.-T. Chen and P. A. Lee, Unified formalism for calculating polarization, magnetization, and more in a periodic insulator, Phys. Rev. B **84**, 205137 (2011).

[58] A. L. R. Manesco, J. L. Lado, E. V. Ribeiro, G. Weber, and J. Rodrigues, Durval, Correlations in the elastic Landau level of a graphene/NbSe$_2$ van der Waals heterostructure, arXiv e-prints (2020), arXiv:2003.05163 [cond-mat.mes-hall].

[59] D. Xiao, W. Yao, and Q. Niu, Valley-contrasting physics in graphene: Magnetic moment and topological transport, Phys. Rev. Lett. **99**, 1 (2007).

[60] M. Yamamoto, Y. Shimazaki, I. V. Borzenets, and S. Tarucha, Valley Hall effect in two-dimensional hexagonal lattices, Journal of the Physical Society of Japan **84**, 121006 (2015).

[61] Y. Jiang, T. Low, K. Chang, M. I. Katsnelson, and F. Guinea, Generation of pure bulk valley current in graphene, Phys. Rev. Lett. **110**, 046601 (2013).

[62] T. L. Linnik, Photoinduced valley currents in strained graphene, Phys. Rev. B **90**, 075406 (2014).

[63] J. H. J. Martiny, K. Kaasbjerg, and A.-P. Jauho, Tunable valley Hall effect in gate-defined graphene superlattices, Phys. Rev. B **100**, 155414 (2019).

[64] V. H. Nguyen, S. Dechamps, P. Dollfus, and J.-C. Charlier, Valley filtering and electronic optics using polycrystalline graphene, Phys. Rev. Lett. **117**, 247702 (2016).

[65] A. R. Akhmerov and C. W. J. Beenakker, Detection of valley polarization in graphene by a superconducting contact, Phys. Rev. Lett. **98**, 157003 (2007).

[66] P. Rickhaus, J. Wallbank, S. Slizovskiy, R. Pisoni, H. Overweg, Y. Lee, M. Eich, M.-H. Liu, K. Watanabe, T. Taniguchi, T. Ihn,

and K. Ensslin, Transport through a network of topological channels in twisted bilayer graphene, Nano Letters **18**, 6725 (2018).

[67] S. G. Xu, A. I. Berdyugin, P. Kumaravadivel, F. Guinea, R. K. Kumar, D. A. Bandurin, S. V. Morozov, W. Kuang, B. Tsim, S. Liu, J. H. Edgar, I. V. Grigorieva, V. I. Fal'ko, M. Kim, and A. K. Geim, Giant oscillations in a triangular network of one-dimensional states in marginally twisted graphene, Nature Communications **10**, 10.1038/s41467-019-11971-7 (2019).

[68] S. Huang, K. Kim, D. K. Efimkin, T. Lovorn, T. Taniguchi, K. Watanabe, A. H. MacDonald, E. Tutuc, and B. J. LeRoy, Topologically protected helical states in minimally twisted bilayer graphene, Phys. Rev. Lett. **121**, 037702 (2018).

[69] Y. Shimazaki, M. Yamamoto, I. V. Borzenets, K. Watanabe, T. Taniguchi, and S. Tarucha, Generation and detection of pure valley current by electrically induced Berry curvature in bilayer graphene, Nature Physics **11**, 1032 (2015).

[70] L. Meng, Z.-D. Chu, Y. Zhang, J.-Y. Yang, R.-F. Dou, J.-C. Nie, and L. He, Enhanced intervalley scattering of twisted bilayer graphene by periodic *AB* stacked atoms, Phys. Rev. B **85**, 235453 (2012).

[71] B. Yan, Q. Han, Z. Jia, J. Niu, T. Cai, D. Yu, and X. Wu, Electrical control of intervalley scattering in graphene via the charge state of defects, Phys. Rev. B **93**, 041407 (2016).

[72] A. F. Morpurgo and F. Guinea, Intervalley scattering, long-range disorder, and effective time-reversal symmetry breaking in graphene, Phys. Rev. Lett. **97**, 196804 (2006).

[73] C. Shen, Y. Chu, Q. Wu, N. Li, S. Wang, Y. Zhao, J. Tang, J. Liu, J. Tian, K. Watanabe, T. Taniguchi, R. Yang, Z. Y. Meng, D. Shi, O. V. Yazyev, and G. Zhang, Correlated states in twisted double bilayer graphene, Nature Physics **16**, 520 (2020).

[74] X. Liu, Z. Hao, E. Khalaf, J. Y. Lee, K. Watanabe, T. Taniguchi, A. Vishwanath, and P. Kim, Spin-polarized Correlated Insulator and Superconductor in Twisted Double Bilayer Graphene, arXiv e-prints (2019), arXiv:1903.08130 [cond-mat.mes-hall].

[75] M. He, Y. Li, J. Cai, Y. Liu, K. Watanabe, T. Taniguchi, X. Xu, and M. Yankowitz, Tunable correlation-driven symmetry breaking in twisted double bilayer graphene, arXiv e-prints (2020), arXiv:2002.08904 [cond-mat.mes-hall].

[76] G. W. Burg, J. Zhu, T. Taniguchi, K. Watanabe, A. H. MacDonald, and E. Tutuc, Correlated insulating states in twisted double bilayer graphene, Phys. Rev. Lett. **123**, 197702 (2019).

[77] A. Abouelkomsan, Z. Liu, and E. J. Bergholtz, Particle-hole duality, emergent Fermi liquids, and fractional Chern insulators in moiré flatbands, Phys. Rev. Lett. **124**, 106803 (2020).

[78] Z. Liu, A. Abouelkomsan, and E. J. Bergholtz, Gate-Tunable Fractional Chern Insulators in Twisted Double Bilayer Graphene, arXiv e-prints (2020), arXiv:2004.09522 [cond-mat.mes-hall].

[79] P. J. Ledwith, G. Tarnopolsky, E. Khalaf, and A. Vishwanath, Fractional Chern Insulator States in Twisted Bilayer Graphene: An Analytical Approach, Physical Review Research **2**, 10.1103/physrevresearch.2.023237 (2020).

[80] C. Repellin and T. Senthil, Chern bands of twisted bilayer graphene: fractional Chern insulators and spin phase transition, Physical Review Research **2**, 10.1103/physrevresearch.2.023238 (2020).

[81] X.-C. Wu, A. Keselman, C.-M. Jian, K. A. Pawlak, and C. Xu, Ferromagnetism and spin-valley liquid states in moiré correlated insulators, Phys. Rev. B **100**, 024421 (2019).

[82] V. Y. Irkhin and Y. N. Skryabin, Dirac points, spinons, and spin liquid in twisted bilayer graphene, JETP Letters **107**, 651 (2018).

[83] L. A. Gonzalez-Arraga, J. L. Lado, F. Guinea, and P. San-Jose, Electrically controllable magnetism in twisted bilayer graphene, Phys. Rev. Lett. **119**, 107201 (2017).

Supplementary Material for
"Spontaneous Valley Spirals in Magnetically Encapsulated Twisted Bilayer Graphene"

MICROSCOPIC TIGHT-BINDING MODEL

For the reader's convenience, here we repeat the generic atomistic tight-binding Hamiltonian for stacked graphene [see Eq. (1) in the main text] with atoms located at coordinates $\{\boldsymbol{r}_i\}$, i.e.,

$$H_0 = \sum_{i \neq j,s} t(\boldsymbol{r}_i - \boldsymbol{r}_j)\, c_{is}^\dagger c_{js} + \sum_{is} V(\boldsymbol{r}_i)\, c_{is}^\dagger c_{is}, \tag{S1}$$

where $c_{is}^{(\dagger)}$ destroys (creates) an electron at site $\boldsymbol{r}_i$ with spin $s \in \{\pm 1/2\}$. The hopping amplitudes can be parametrized as Slater-Koster transfer integrals between the atomic orbitals [S1, S2], i.e.,

$$-t(\boldsymbol{R}) = t_{pp\pi}(R) \cdot \left(1 - \left(\frac{\boldsymbol{R} \cdot \hat{z}}{R}\right)^2\right) + t_{pp\sigma}(R) \cdot \left(\frac{\boldsymbol{R} \cdot \hat{z}}{R}\right) \tag{S2}$$

with decaying overlap amplitudes $t_{pp\pi} = t\, e^{-(R-a_0)/\ell}$ and $t_{pp\sigma} = t_\perp\, e^{-(R-d)/\ell}$ where $a_0 = a/\sqrt{3} \approx 0.142$ nm is the intralayer interatom distance, $d \approx 2.35 a_0$ is the interlayer spacing, $t \approx 2.7$ eV is the first-neighbor transfer integral and $t_\perp \approx -0.18t$ is interlayer transfer integral, and $\ell \approx 0.33 a_0$ is the decay length of the overlap integrals. In our case, the onsite potential

$$V(\boldsymbol{r}) = \mu + \mathrm{sign}(z_i)\, V \tag{S3}$$

contains the overall chemical potential μ and the interlayer bias V.

As explained in the main text, the presence of a ferromagnetic insulator (FI) introduces an effective exchange field, such that the the electron spin couples to an effective magnetic moment $\boldsymbol{m}(\boldsymbol{r})$, i.e.,

$$H_{\mathrm{J}} = \sum_{jss'} (\boldsymbol{m}(\boldsymbol{r}_j) \cdot \boldsymbol{\sigma})_{ss'} c_{js}^\dagger c_{js'}, \tag{S4}$$

where $\boldsymbol{\sigma} = (\sigma_x, \sigma_y, \sigma_z)$ are the spin Pauli matrices. We assume that the FI is layer-antiferromagnetic, i.e., $\boldsymbol{m}(\boldsymbol{r}) = \mathrm{sign}(z_i) m\, \hat{z}$. The FI also induces the Rasbha spin–orbit interaction

$$H_{\mathrm{R}} = \sum_{\langle ij\rangle, ss'} i\lambda_{\mathrm{R}}(\boldsymbol{r}_i)(\boldsymbol{\sigma} \times \boldsymbol{d}_{ij})_{ss'}^z\, c_{is}^\dagger c_{js'}, \tag{S5}$$

where $\boldsymbol{d}_{ij}$ is the bond vector connecting intralayer sites i, j. The Rasbha spin–orbit coupling in this case is $\lambda_{\mathrm{R}}(\boldsymbol{r}) = \mathrm{sign}(z_i)\lambda_{\mathrm{R}}$.

If we now consider the Hamiltonian $H = H_0 + H_{\mathrm{J}} + H_{\mathrm{R}}$ twisted bilayer graphene at fixed physical parameters t, $t_\perp$, m and λ_{R}, the electronic spectrum still depends on the twist angle α. We can investigate this dependence by considering the density of states, to identify van Hove singularities and band gaps, see Fig. S1. Note that it is generally computationally expensive to vary the twist angle in the tight-binding calculation. However, a rescaling argument in the parameter $\alpha/t_\perp$ can be used to vary the interlayer hop amplitude at fixed angle instead [S2].

FERMI-HUBBARD MODEL

Hamiltonian

In the main text, we consider a generalized Fermi-Hubbard model describing hopping between effective electronic orbitals that are punished by local on-site repulsion [c.f. Eqs. (2) and (3) in the main text]. In our case, the spin degree of freedom is hybridized and valleys K, K' take the role of a pseudospin degree of freedom, which we will denote with $v = \pm 1/2$. The corresponding Hamiltonian is

$$\mathcal{H} = \mathcal{H}_t + \mathcal{H}_U = \sum_{i \neq j, v = \pm 1/2} t_{ij}^v\, d_{iv}^\dagger d_{jv} + \frac{U}{2} \sum_{i,v} n_{iv} n_{i(-v)}, \tag{S6}$$

where $n_{iv} = d_{iv}^\dagger d_{iv}$ is the local number operator with creation/annihilation operators $\{d_{iv}, d_{jv'}^\dagger\} = \delta_{ij}\delta_{vv'}$, and $U > 0$ is the Hubbard interaction strength. In particular, we allow valley-dependent hopping amplitudes $t_{ij}^v = t_{ij}^{\mathrm{s}} + v\, t_{ij}^{\mathrm{a}}$.
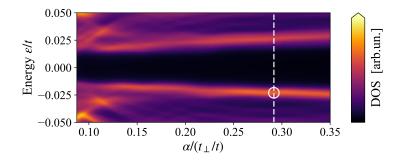
FIG. S1. Density of states of FI-encapsulated twisted bilayer graphene for different interlayer hopping amplitudes as a function of $\alpha/t_\perp$ (calculated with $\alpha \approx 2°$ fixed, $t_\perp/t \in [0.1, 0.4]$) with $m = \lambda_R = 0.33t_\perp$. The dashed line and circle indicate the van Hove singularity associated to the flat band investigated in the main text.

Symmetry

The configuration of the ferromagnetic insulators in the microscopic model (see main text) allows us to introduce the combination of time reversal and structural symmetry operations as pseudo-time-reversal symmetry operation. In our Fermi-Hubbard model, this symmetry operation is then given by $\mathcal{T} = i\sigma_y \mathcal{K}$, where $\mathcal{K}$ denotes complex conjugation. This symmetry implies $t_{ij}^v = (t_{ij}^{-v})^*$, which is equivalent to

$$t_{ij}^v = \gamma_{ij} e^{iv\phi_{ij}} \qquad \text{with} \qquad \gamma_{ij} = \gamma_{ji} > 0, \quad \phi_{ij} = -\phi_{ji} \in [0, 2\pi] \tag{S7}$$

due to hermaticity. These hopping amplitudes lend themselves to an interpretation as pseudospin–orbit coupling (or "valley–orbit" coupling), which can be seen for example by looking at the Kane-Mele model [S3]. In the main text, we restricted ourselves to first- and second-neighbor amplitudes, i.e.,

$$t_{\langle ij \rangle}^v = \gamma_1 e^{iv\varepsilon_{ij}\phi_1} \quad \text{and} \quad t_{\langle\langle ij \rangle\rangle}^v = \gamma_2 e^{iv\nu_{ij}\phi_2}, \qquad \text{where} \qquad \nu_{ij} \in \{\pm 1, 0\}$$

is antisymmetric and also restricted by structural symmetries.

Introducing the spinor $\psi_i = (d_{i\uparrow}, d_{i\downarrow})$, we can also define spin operators $v_{i\alpha} = (1/2)\psi_i^\dagger \sigma_\alpha \psi_i$, where σ_α are the Pauli matrices ($\alpha = x, y, z$). These transform as $\boldsymbol{v}_i \mapsto R\boldsymbol{v}_i$ under spinor rotations $\psi_i \mapsto U\psi_i = \exp(i\varphi\boldsymbol{n} \cdot \boldsymbol{\sigma}/2)\psi_i$, where R is the spin rotation associated to the spinor rotation U. Our Hamiltonian H then has the symmetry axis $\boldsymbol{n} = \boldsymbol{e}_z$. Furthermore, the mirror operation $U = i\sigma_x$ is a symmetry if $t_{ij}^v = t_{ij}^{-v}$. The latter paired with time reversal symmetry implies $\phi_{ij} = 0, \pm\pi/2, \pi$. Note that this mirror operation is generally *not* a symmetry of our Hamiltonian.

Hartree-Fock mean field approximation

We introduce the mean density matrix $\rho_{vv'}^i = \langle d_{iv}^\dagger d_{iv'} \rangle$ and use the mean field approximation [S4] to find

$$\mathcal{H}_U \approx \mathcal{H}_U(\rho) = U \sum_{iv} \underbrace{\rho_{(-v)(-v)}^i c_{iv}^\dagger c_{iv}}_{\text{Hartree}} - \underbrace{\rho_{(-v)v}^i c_{iv}^\dagger c_{i(-v)}}_{\text{Fock}} + \frac{U}{2} \underbrace{\sum_{iv} \rho_{vv}^i \rho_{(-v)(-v)}^i - |\rho_{v(-v)}^i|^2}_{\equiv \sum_i E_0(\rho^i)}$$

$$= \sum_{ivv'} \bar{U}_{vv'}(\rho^i) \, c_{iv}^\dagger c_{iv'} + \sum_i E_0(\rho^i), \tag{S8}$$

where $\bar{U}_{vv'}(\rho^i) = U \delta_{vv'} \rho_{(-v)(-v)}^i - U \delta_{v(-v')} \rho_{(-v)v}^i$. The density matrix ρ^i is then obtained through the self-consistency relation

$$\rho_{vv'}^i = \langle d_{iv}^\dagger d_{iv'} \rangle \approx Z^{-1}(\rho) \, \text{tr} \left[e^{-\beta\mathcal{H}(\rho)} c_{iv}^\dagger c_{iv'} \right],$$

which must be solved numerically (e.g., through fixed point iteration). The expectation value of the valley operator can then be extracted by observing that $\rho^i = \frac{1}{2} (\langle n_i \rangle + \langle \boldsymbol{v}_i \rangle \cdot \boldsymbol{\sigma})$, where $n_i = \sum_v n_{iv}$ is the occupation number at site i.

EFFECTIVE VALLEY–VALLEY EXCHANGE INTERACTIONS

In the large-U limit of the Fermi-Hubbard model $\mathcal{H}$, the hoppings $\mathcal{H}_t$ can be included in second-order perturbation theory, or equivalently by using the Schrieffer-Wolff transformation that eliminates the hoppings to first order via the canonical transformation [S5, S6]

$$\mathcal{H}' = e^{-A}\mathcal{H}e^A \approx \mathcal{H} - [A, \mathcal{H}] + \frac{1}{2}[A, [A, \mathcal{H}]] + \ldots \approx \mathcal{H}_U - \frac{1}{2}[A, \mathcal{H}_t] + \mathcal{O}(t^3),$$

where A is chosen such that $\mathcal{H}_t - [A, \mathcal{H}_U] = 0$. The last constraint is solved in the subspace of states for which each lattice site is singly occupied (most relevant for large U at half-filling). Denoting the corresponding subspace projector P (and its orthogonal complement $P_\perp$), one can show that $A = (P\mathcal{H}_t P_\perp - P_\perp \mathcal{H}_t P)/U$ leads to

$$\mathcal{H}_v \equiv PH'P = -PH_t^2 P = -P \sum_{i \neq j, vv'} \frac{t_{ij}^v (t_{ij}^{v'})^*}{U} d_{jv'}^\dagger d_{iv'} d_{iv}^\dagger d_{jv} P, \tag{S9}$$

which after some manipulations and using $v_{i+} = d_{i(1/2)}^\dagger d_{i(-1/2)} = v_{ix} + iv_{iy} = (v_{i-})^\dagger$ and $v_{iz} = (n_{i(1/2)} - n_{i(-1/2)})/2$ leads to an anisotropic Heisenberg model with antisymmetric exchange, i.e.,

$$H_v = \sum_{i \neq j, v} J_{ij} \boldsymbol{v}_i \cdot \boldsymbol{v}_j + \Delta_{ij} v_{iz} v_{jz} + D_{ij} \boldsymbol{z} \cdot (\boldsymbol{v}_i \times \boldsymbol{v}_j) + \text{const.},$$

with the exchange couplings

$$J_{ij} = J_{ij}^0 \pm \frac{\Delta_{ij}}{2} = \frac{2\left|t_{ij}^s\right|^2}{U} - \frac{2\left|t_{ij}^a\right|^2}{U} = \frac{2\gamma_{ij}^2}{U}(\cos^2\phi_{ij} - \sin^2\phi_{ij}), \tag{S10}$$

$$\Delta_{ij} = \frac{4\left|t_{ij}^a\right|^2}{U} = \frac{4\gamma_{ij}^2}{U}\sin^2\phi_{ij}, \tag{S11}$$

$$D_{ij} = \frac{4\,\text{Im}\left[t_{ij}^s\left(t_{ij}^a\right)^*\right]}{U} = \frac{2\gamma_{ij}^2}{U}\sin(2\phi_{ij}). \tag{S12}$$

Note that this Hamiltonian $\mathcal{H}_v$ is compatible with the spinor rotation symmetry $U_\varphi = \exp(i\varphi\sigma_z/2)$, i.e., around the axis $\boldsymbol{n} = \boldsymbol{e}_z$ – just like the full Hamiltonian $\mathcal{H}$ (S6). Additionally imposing mirror symmetry in spinor space would lead to $\phi_{ij} = 0, \pi$ with $J_{ij} = 2\gamma_{ij}^2/U$ and $\Delta_{ij} = D_{ij} = 0$ or else $\phi_{ij} = \pm\pi/2$ with $J_{ij} = -2\gamma_{ij}^2/U$, $\Delta_{ij} = 4\gamma_{ij}^2/U$ and $D_{ij} = 0$.

Extracting effective valley exchange couplings from mean field

The effective exchange couplings J_{ij}, Δ_{ij} and D_{ij} derived in the strong-U limit, see Eq. (S10), can also be extracted directly from the Hubbard model (S6) using numerical mean field calculations. To this end, we compare ground state energies of the same trial states (i.e. valley-polarized in-plane, valley-polarized out-plane and spin spirals). For example, the difference between ground state energies of trial states polarized in-plane and those out-plane yields the anisotropic coupling Δ_{ij}. The other couplings can be obtained in a similar fashion.

[S1] P. Moon and M. Koshino, Optical absorption in twisted bilayer graphene, Phys. Rev. B **87**, 205404 (2013).

[S2] T. M. R. Wolf, J. L. Lado, G. Blatter, and O. Zilberberg, Electrically tunable flat bands and magnetism in twisted bilayer graphene, Phys. Rev. Lett. **123**, 096802 (2019).

[S3] C. L. Kane and E. J. Mele, Quantum spin hall effect in graphene, Phys. Rev. Lett. **95**, 226801 (2005).

[S4] Note that we use $c_\mu^\dagger c_\nu^\dagger c_\nu c_\mu \approx \rho_{\mu\mu} c_\nu^\dagger c_\nu + \rho_{\nu\nu} c_\mu^\dagger c_\mu - \rho_{\mu\nu} c_\nu^\dagger c_\mu - \rho_{\nu\mu} c_\mu^\dagger c_\nu - \rho_{\mu\mu}\rho_{\nu\nu} + \rho_{\mu\nu}\rho_{\nu\mu}$, where $\rho_{\mu\nu} = \langle c_\mu^\dagger c_\nu \rangle$ for indices μ, ν.

[S5] A. Altland and B. D. Simons, *Condensed matter field theory* (Cambridge university press, 2010).

[S6] J. Spalek, t-J model then and now: A personal perspective from the pioneering times, (2007), arXiv:0706.4236.